

# Trapping Fermionic $^{40}\text{K}$ and Bosonic $^{87}\text{Rb}$ on a Chip

S. Aubin,<sup>1</sup> M. H. T. Extavour,<sup>1</sup> S. Myrskog,<sup>1</sup> L. J. LeBlanc,<sup>1</sup> J. Estève,<sup>2</sup>  
S. Singh,<sup>1</sup> P. Scrutton,<sup>1</sup> D. McKay,<sup>1</sup> R. McKenzie,<sup>1</sup> I. D. Leroux,<sup>1</sup>  
A. Stummer,<sup>1</sup> and J. H. Thywissen<sup>1</sup>

<sup>1</sup>McLennan Physical Laboratories, University of Toronto, Toronto, Ontario, M5S 1A7 Canada

<sup>2</sup>Laboratoire de Photonique et de Nanostructures, UPR 20 du CNRS, 91460 Marcoussis,  
France

E-mail: joseph.thywissen@utoronto.ca; <http://www.physics.utoronto.ca/~jhtgroup/>

(Received February 8, 2005)

*We demonstrate the loading of a Bose–Fermi mixture into a microfabricated magnetic trap. In a single-chamber vacuum system, laser-cooled atoms are transported to the surface of a substrate on which gold wires have been microfabricated. The magnetic field minimum formed near these current-carrying wires is used to confine up to  $6 \times 10^4$  neutral  $^{40}\text{K}$  atoms. In addition, we can simultaneously load  $2 \times 10^5$   $^{87}\text{Rb}$  atoms, demonstrating the confinement of two distinct elements with such a trap. In a sequence optimized for  $^{87}\text{Rb}$  alone, we observe up to  $1 \times 10^7$  trapped atoms. We describe in detail the experimental apparatus, and discuss prospects for evaporative cooling towards quantum degeneracy in both species.*

**KEY WORDS:** Ultracold atoms; magnetic trapping; microfabrication; Bose–Einstein condensation; Fermi degenerate gas; micro-electromagnet.

## 1. INTRODUCTION

Since the observation of Bose–Einstein condensation<sup>1</sup> and Fermi degenerate gases,<sup>2</sup> atomic gases have been used to study quantum degenerate many-body systems. Experiments have demonstrated exquisite control over the trapping environment, temperature, density, and interaction strength of the constituents. In contrast to solid state and liquid systems, quantum degenerate gases are dilute and without impurities, making them more easily compared to theoretical models. Furthermore, observations can be made with spatial imaging or with momentum spectroscopy, both

of which can be done rapidly enough to observe the dynamics of the system. These systems can be tailored to access interesting many-body phenomena such as the Hubbard model,<sup>3</sup> Anderson localization,<sup>4</sup> and the BEC-BCS crossover regime.<sup>5</sup>

Microfabrication of magnetic trapping elements brings new tools to the study of ultra-cold quantum gases.<sup>6,7</sup> Micro-electromagnets ( $\mu$ EMs) can be used to build smaller traps, achieve stronger trap gradients and curvatures,<sup>8</sup> and reduce the power dissipation of the trapping elements. In addition, microfabrication techniques make integration with waveguides<sup>9</sup> and other devices<sup>10,11</sup> possible. The ability to trap atoms near a surface has led to a range of recent studies focusing on interactions between degenerate atom clouds and surfaces.<sup>12,13</sup> To date,  $\mu$ EMs have only been used to study thermal and degenerate Bose gases.

In this paper we discuss an apparatus built to study ultra-cold Fermi gases in a  $\mu$ EM trap. The high oscillation frequency accessible in a strongly confining  $\mu$ EM trap has several advantages for studies of quantum gases. First, an increased collision rate allows fast evaporative cooling, which simplifies the realization of a dual species system, as described in Section 2. Second, the high oscillation frequency allows quantum degeneracy with a smaller number of atoms. The Fermi temperature in a three-dimensional harmonically trapped gas is

$$T_F = \frac{\hbar\omega}{k_B} (6N)^{\frac{1}{3}}, \quad (1)$$

where  $\omega$  is the mean oscillation frequency, and  $N$  is the atom number. At fixed  $T/T_F$ ,  $N$  is proportional to  $\omega^{-3}$ , so higher oscillation frequencies make possible the study of quantum degenerate gases with smaller atom numbers. Systems with small numbers of trapped fermions are reminiscent of quantum dots, where small numbers of electrons are captured in electrostatic wells. Mesoscopic *neutral* Fermi gas samples are also expected to exhibit rich physical phenomena. While Coulomb interactions dominate electron mesoscopics, the relatively weaker interaction energies of neutral Fermi systems facilitate the study of purely quantum-statistical effects such as spatial shell structure.<sup>14</sup>

Another appealing feature of  $\mu$ EM traps is the variety of trap geometries which can be formed. Single traps with a high aspect ratio ( $>10^3$ ) could be used to study quasi-one-dimensional ensembles of fermions<sup>15</sup> or of Bose-Fermi mixtures.<sup>16</sup> Two or more traps could be connected through quantum point contacts<sup>17</sup> or tunneling barriers.

In the following sections, we describe our progress towards realizing some of the experiments mentioned above using bosonic  $^{87}\text{Rb}$  and fermionic  $^{40}\text{K}$ . After a description of the apparatus in Section 2, we discuss

its performance to date in Section 3, which includes the first demonstration, to our knowledge, of trapping fermions in a  $\mu\text{EM}$  trap. We discuss prospects for evaporative cooling towards quantum degeneracy in both species and our experimental outlook in Section 4.

## 2. EXPERIMENTAL APPARATUS

Experiments with quantum degenerate gases require *trapping*, *cooling*, and *imaging* of ultra-cold atoms. In our case, trapping is accomplished by capturing atoms from a background vapor in a Magneto-Optical Trap (MOT), and then transferring them to a purely magnetic trap, both within the same vacuum chamber. Cooling is accomplished in two steps: first, by laser cooling in the MOT and with optical molasses; second, by forced evaporative cooling in the  $\mu\text{EM}$  magnetic trap. Imaging is either fluorescent or absorptive, using resonant laser light and CCD cameras in both cases.

Our system is vastly simplified by the use of a  $\mu\text{EM}$  trap. The evaporative cooling times realized in such traps are typically a few seconds,<sup>6,13,18,19</sup> short enough that a single vacuum chamber can be used both to collect atoms from the background vapor and to cool them to degeneracy with evaporative cooling. Systems with magnetic traps created by standard coils require multiple chambers (or Zeeman slower) to maintain an ultra-high vacuum. Additional lasers are then typically required to move atoms between chambers (or slow them). In a dual-species experiment such as ours, additional lasers would be required for both species. The single-chamber configuration possible with a  $\mu\text{EM}$  trap avoids the above complications.

The following subsections describe the essential components of the experiment, sometimes focusing on technical choices that we believe would be interesting to researchers in the field. For a more general audience, this description can serve as a specific example of a degenerate gas experiment that is structurally similar to many other existing experiments. We also refer the reader to review articles of experimental techniques.<sup>20</sup>

### 2.1. Vacuum System

The required quality of the vacuum environment of the trap is in general dictated by the desired lifetime of the trapped atoms. A collision with a background atom or molecule (thermalized with the walls of the chamber at room temperature) can eject an atom from the trap, since the energy transferred is generally much higher than the trap depth (between 1 K and 1 mK). For a 10 s  $1/e$  lifetime for rubidium, for instance, the partial

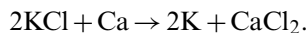
pressure of hydrogen must be no higher than  $3 \times 10^{-9}$  mbar.<sup>21</sup> A vacuum environment also serves to thermally isolate the cold gases from ambient temperature, since convective and conductive heat transfer are eliminated by working in a vacuum.<sup>22</sup>

Our vacuum system consists of a Pyrex cell, 75 mm  $\times$  75 mm  $\times$  165 mm, connected to an ion pump and a titanium sublimation pump through a 6 inch conflat stainless steel cube a turbo pump is connected to the system, during pump-down and bake-out, but sealed off using a gate valve during normal operation.<sup>23</sup> The entire system is supported on an optical table in such a way that the glass cell is closest to the table. Magnetic trap (see Section 2.4) lifetimes as long as 9 s and MOT lifetimes as long as 24 s have been observed, suggesting that the pressure in the system is at or below  $4 \times 10^{-9}$  mbar.

## 2.2. Sources

Alkali atoms – both rubidium and potassium – are selectively released into the vacuum chamber using dispenser sources.<sup>24</sup> These devices use a reaction between an alkali salt and a reducing agent to produce free alkali atoms and a byproduct. The reaction is activated by resistive heating of the nichrome envelope in which the reactants are housed.

Dispensers are commercially available<sup>25</sup> for both rubidium and potassium in their natural isotopic abundance. While the natural abundance of  $^{87}\text{Rb}$  (27.83%) is acceptably high, the natural abundance of  $^{40}\text{K}$  is only 0.012%. We use a commercial rubidium dispenser but have constructed a potassium dispenser using an isotope-enriched potassium salt. Our dispenser was modeled after that of Ref. 26, with the addition of a fine nickel mesh to contain the reactants. The device uses the following heat-enhanced reaction to supply potassium:



Using hot wire tests, we estimate that our isotope-enriched dispenser can produce 100  $\mu\text{g}$  of fermionic potassium. Given our typical  $^{40}\text{K}$  MOT size of  $10^7$  atoms (discussed in Section 3.2), it is reasonable to expect the dispenser lifetime to be on the order of years, as has been observed in other degenerate gas experiments.

Although some atoms dispensed by our sources are trapped in the MOT, most are deposited on the walls of the glass cell or captured by the vacuum pumps. We observe that  $^{87}\text{Rb}$  atoms can be “recycled” from the glass walls using light-induced atom desorption (LIAD).<sup>27,28</sup> Whereas previous observations of this effect in cold atom experiments have used

broadband white light sources,<sup>6,29</sup> we observe wavelength dependence of the  $^{87}\text{Rb}$  desorption efficiency.<sup>30</sup>

With the dispensers off, we measured the number of  $^{87}\text{Rb}$  atoms captured by the MOT as a function of the center wavelength of various weak ( $\sim 0.5\text{ mW}$ ) LED sources of desorbing light. Wavelengths greater than 500 nm had no visible effect, whereas wavelengths in the 400 nm range boosted the MOT loading rate by a factor of five. This is consistent with observations in paraffin-coated vapor cells,<sup>28</sup> although it is unknown if the LIAD mechanism is identical. Encouraged by these preliminary tests, we built a 140 mW source at a center wavelength of 405 nm. Desorption using this source allows us to load  $10^9$   $^{87}\text{Rb}$  atoms into the MOT without turning on the dispensers,<sup>31</sup> which reduces the background pressure and increases the trap lifetime. The atom number we capture with LIAD in a UHV cell is 100 times larger than without LIAD, and over 10 times larger than that reported in previous experiments,<sup>6,19</sup> where higher power white light sources were used. This comparison may not be an accurate measure of the source efficiency, since our MOT uses much larger trapping beams. Nonetheless, LIAD allows us to load large MOTs while maintaining a better vacuum for longer magnetic trap lifetimes.

### 2.3. Laser System

Near-resonant lasers are used for laser cooling and trapping, optical pumping, and imaging. These applications require laser linewidths that are small compared to the natural atomic linewidth ( $\Gamma \approx 2\pi \times 6\text{ MHz}$  for the cycling transitions in  $^{40}\text{K}$  and  $^{87}\text{Rb}$ ) and sufficient power to saturate the cooling transition in our MOT. These constraints are met by locking low-power grating-stabilized diode lasers, injecting into free-running seed lasers, passing the light through single-mode optical fibers, and where necessary, injecting into a tapered amplifier as a second stage of amplification, as shown in Fig. 1. The fiber optics produce clean spatial modes for imaging beams, and decouple the alignment of the beams around the vacuum system from other, less critical alignments.

Four master lasers are used: two for the  $^{87}\text{Rb}$   $D_2$  line at 780.246 nm, and two for the  $^{40}\text{K}$   $D_2$  line at 766.702 nm. Of each pair, one laser is tuned to the cycling transition (i.e., from the  $5S_{1/2} F=2$  ground state to the  $5P_{3/2} F'=3$  excited state for  $^{87}\text{Rb}$ , and from the  $4S_{1/2} F=9/2$  ground state to the  $4P_{3/2}$  excited state manifold for  $^{40}\text{K}$ ) and the other laser to the repumping transition (out of the  $F=1$  ground state for  $^{87}\text{Rb}$  and out of the  $F=7/2$  ground state for  $^{40}\text{K}$ ). The ground state hyperfine splittings are 6.835 and 1.286 GHz for  $^{87}\text{Rb}$  and  $^{40}\text{K}$  respectively, large enough that separate master lasers are convenient.

These resonant wavelengths are an ideal combination for a two-species experiment.<sup>32</sup> They are close enough that they can share the same mirrors, fibers, coatings, and tapered amplifier (whose bandwidth is 23 nm), but far enough apart that dichroic waveplates can selectively manipulate the polarization of one wavelength without affecting the other, such that 100% combining efficiency can be achieved.

Each master is locked using saturated absorption spectroscopy. A modulation transfer scheme is used, in which the frequency of the pump is dithered (in our case, at 100 kHz) and the resultant amplitude modulation of the probe is used to lock to a peak maximum. The output of a lock circuit is sent both to the piezo voltage and to the current of the master laser, to achieve a lock bandwidth of over 5 kHz. Using this method, we observe a short term stability of 300 kHz. Three of these master lasers (all but the Rb repump) inject room-temperature free-running diode lasers to boost their power.

Figure 1 shows the mixing of various frequencies into the fiber optics that transport them to the vacuum system. The majority of the laser power is injected into the tapered amplifier, producing 0.65 W of output power after spatial filtering, which is split into six beams for the MOT. A second fiber is used for imaging, which is described in more detail in Section 3.1. A third fiber is used for optical pumping into a specific magnetic sublevel to maximize efficiency of loading from the MOT (which traps all states) into the magnetic trap (which traps only specific sublevels). In all cases, dichroic waveplates<sup>33</sup> are used to produce a single polarization of light.

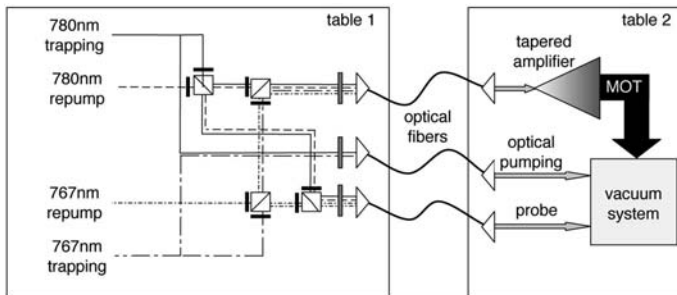


Fig. 1. A schematic showing the splitting and combining of the various optical frequencies according to their function and desired path through the vacuum chamber. Polarizing beam splitter cubes, broadband waveplates (black), and dichroic wave plates (grey) are shown. Single-mode optical fibers send light to the vacuum system. One of these fibers injects the tapered amplifier, which produces the MOT beams. The other fiber paths are aligned directly into the pyrex vacuum cell. Additional frequency modifications by acousto-optic modulators are not shown.

## 2.4. Magnetic Trap

Two pairs of circular coils are used to create the magnetic field for the MOT, for the first magnetic trap, and for the movement of the magnetically trapped atoms from the first magnetic trap (formed at the MOT) to the chip trap 5 cm away. As shown in Fig. 2, all four coils are mounted outside the glass cell. The inner pair of coils (the ‘‘MOT coils’’) create the linear quadrupole fields for the MOT and magnetic trap. Both MOT coils consist of 100 turns of insulated, hollow-core<sup>34</sup> copper wire, wound to form a square cross-section with an inner (outer) diameter of 10 cm (18.4 cm). The coils are mounted with an inner separation of 8.4 cm. The outer coils (the ‘‘Transfer coils’’) carry equal and parallel currents to provide a nearly uniform field in the  $z$  direction. They are made of the same hollow-core copper wire, but have 49 turns each and inner (outer) diameters of 28 cm (36.4 cm). The Transfer coils are mounted with an inner separation of 11.4 cm. Applying the uniform field of the Transfer coils to the quadrupole field of the MOT coils shifts the location of the  $B = 0$  trap center along the  $z$  axis (vertical). The MOT laser beams are aligned so that they intersect at  $z = -2.5$  cm from the center of the MOT coils.

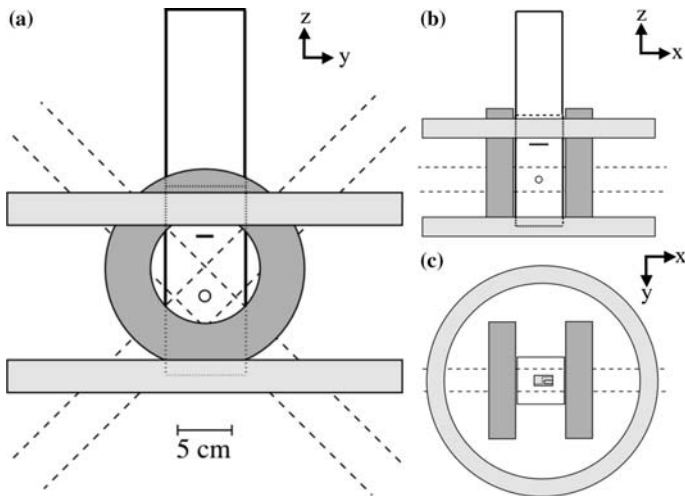


Fig. 2. Glass cell, MOT coils. Transfer coils, atom chip, and MOT beams as seen along (a) the  $x$  axis, (b) the  $y$  axis; and (c) the  $z$  axis. Coils (shaded) are positioned around the glass vacuum cell (solid lines). Diagonal ( $\hat{y} \pm \hat{z}$ ) MOT beams are shown (dashed) only in (a); horizontal ( $\hat{x}$ ) MOT beams are shown in both (b) and (c). The atom chip is seen face-on in (c) and indicated with a thick black line in (a) and (b).

Together, these coils create and move the trap center between the location of the MOT and the surface of the chip, several centimeters away.

The advantage of this “off-center” MOT is power efficiency. A strong quadrupole trap can only be formed within roughly half a coil radius of the center of a pair of anti-Helmholtz coils. Had we formed the MOT at the center of the coils and transported the atoms the same distance to the chip, the radius of the coils would have been doubled. Maintaining the same magnetic field gradient in these larger coils would require an order of magnitude more electrical power.

As built, the power consumption for the primary coils is 0.8 kW at 60 A, which generates a gradient of 94 G/cm along the  $\hat{x}$ -axis. Optical access is sufficient for six 5-cm-diameter MOT beams. Using the Transfer coils, cold atoms have been transported over 5.5 cm.

## 2.5. Trap Switch

Several phases of the experiment require fast switching of the magnetic trap coils. In order to load atoms from the MOT into the magnetic trap, the coils must be turned off quickly to create a zero-field condition for optical molasses, and then turned on quickly to high current for efficient loading of the magnetic trap. Fast turn-off is also necessary when imaging the atoms in order to avoid heating, distortion of the cloud, and Zeeman shifts of the atomic energy levels. The necessary time scale is determined by the motion of atoms in the trap: fields should be switched in less time than a single classical oscillation period. A chip trap (see Section 2.6) can have oscillation frequencies above 1 kHz, requiring sub-ms switching times for its bias fields. At 3 mH inductance and 60 A of current, voltages up to 1 kV are required to achieve sufficiently fast switching times.

Fig. 3a shows a schematic of the control circuit (dubbed “Mag-O-Matic”) for rapidly switching large currents. The complete trap requires two such switches: one for the MOT and one for the Transfer coil. These are independent and nearly identical; only the MOT control circuit is shown. The difference between the two circuits is the role of the relay: the Transfer coils are hard-wired in series, but the relay determines the direction of current; the relay in the MOT circuit switches the coils between Helmholtz and anti-Helmholtz configurations.

When the coils are operating in steady state, the IGBT (Insulated Gate Bipolar Junction Transistor) stack is on and the coil supplies are running in constant current mode. The current flows through the blocking diode, the coils, the IGBT stack, and a giant magneto-resistive (GMR) current sensor. The sensor is used for quantitative monitoring only.



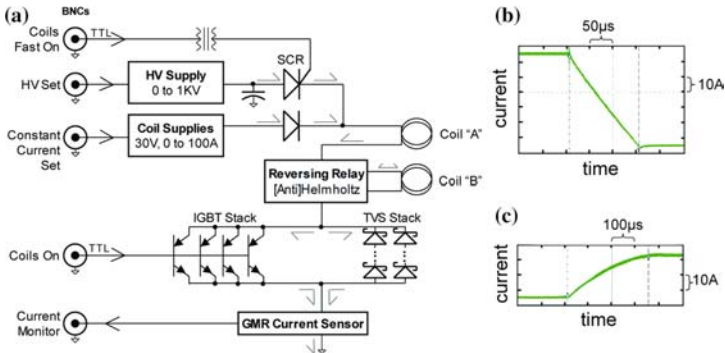


Fig. 3. (a) Magnetic trap switch for the MOT coils. The primary switch is a stack of Insulated Gate Bipolar junction Transistors (IGBT's). Turn-on is accelerated with a high voltage (HV) charge in a capacitor, whose discharge is triggered using a Silicon Controlled Rectifier (SCR). Turn-off is accelerated with transient voltage suppressors (TVS's). Current is sensed using a giant magneto-resistive (GMR) current sensor. Arrows indicate the direction of controls and monitors; half arrows indicate coil currents. (b) Turn-off performance: current falls from 60 A to zero in 150  $\mu\text{s}$ . (c) Turn-on performance: rise of current from 0 to 26.5 A in 350  $\mu\text{s}$ .

The coils are turned off by turning the IGBT stack off. The counter-EMF (or “flyback”) caused by the inductance of the coils produces a high voltage spike which is clamped by the transient voltage suppressors (TVS) at about 940 V. The coil current is dissipated at 0.4 A/ $\mu\text{s}$ , as shown in Fig. 3b.

There are two ways to turn on the coil current. If the IGBT stack alone is turned on, the current will rise asymptotically to the steady-state value in  $\sim 20$  ms. The other turn-on method (the “fast on”) works as follows. At any time before the fast turn-on is needed, the high voltage (HV) supply is used to charge up the HV capacitor. Fast turn-on is triggered by first turning on the IGBT stack, and then triggering the HV Silicon Controlled Rectifier (SCR). In the few microseconds between these two events, no significant current flows due to the coil inductance. Triggering the SCR creates an LC parallel resonant circuit with the coil inductance and the HV capacitor. During the first quarter-cycle of the resonance, roughly 350  $\mu\text{s}$ , the capacitor transfers its charge to the coil (see Fig. 3c). The charge on the capacitor is chosen such that after this quarter-cycle the coil is at its steady state voltage, and the blocking diode of the supplies will conduct to provide the steady state current. The SCR turns off when the current flowing through it falls to zero.

## 2.6. Atom Chip

Although the external magnetic trap described in Section 2.4 can capture and hold the atoms, efficient evaporative cooling requires a collision rate that is several hundred times greater than the loss rate from the trap.<sup>35</sup> In our single-chamber vapor cell, the loss rate is roughly  $0.2\text{ s}^{-1}$ . As a result, the initial collision rate must be greater than  $10^2\text{ s}^{-1}$ , which (for the number and temperature typically captured by a MOT) requires a more tightly confining trap than our external coils can provide.

A  $\mu\text{EM}$  trap (or “atom chip”) can provide much stronger confinement – while using smaller currents – than a trap produced by conventional coils.<sup>8</sup> To understand this, consider a cylindrical wire of diameter  $D$  carrying current  $I$ . The field gradient at a distance  $r > D/2$  from the wire is

$$B' = -\frac{\mu_0 I}{2\pi r^2}, \quad (2)$$

where  $\mu_0$  is the permittivity of free space. Decreasing the wire radius decreases the minimum  $r$  but also decreases the current capacity<sup>36</sup>  $I$  as  $D^{3/2}$ , and thus the maximum gradient scales as  $D^{-1/2}$ . Reducing  $D$  from millimeter-scale to micrometer-scale therefore improves the magnetic field gradient by several orders of magnitude. This higher gradient provides tighter confinement, which increases the collision rate and accelerates the thermalization necessary for evaporative cooling.

The atom chip we are using for this experiment is identical to the one described in Ref. 18. Two types of traps are used: a “U-trap” and a “Z-trap”. These configurations, along with the external field necessary to form a trap near the wire, are shown in Fig. 4.

The U-trap consists of a  $420\text{-}\mu\text{m}$ -wide,  $7\text{-}\mu\text{m}$ -high gold wire in the shape of the letter ‘U’, as shown in Fig. 4a. The base of the U is  $2.0\text{ mm}$  long. When a bias field is applied parallel to the plane of the U and perpendicular to its base, a three-dimensional quadrupole trap is formed above the base of the wire. Using a current of  $5.0\text{ A}$  and a bias field of  $20\text{ G}$ , a quadrupole trap is formed  $430\text{ }\mu\text{m}$  from the surface, with a trap depth of  $1.3\text{ mK}$ , and a mean gradient of  $200\text{ G/cm}$ .

The Z-trap consists of a  $60\text{-}\mu\text{m}$ -wide,  $7\text{-}\mu\text{m}$ -high gold wire in the shape of the letter ‘Z’, as shown in Fig. 4b. The middle segment of the Z is  $2.85\text{ mm}$  long. When a bias field is applied to this wire, a Ioffe-Pritchard-type trap (i.e., a magnetic trap whose minimum field is nonzero) is formed above the surface. Using a current of  $2.0\text{ A}$  and a bias field of  $40\text{ G}$ , the minimum is  $100\text{ }\mu\text{m}$  from the surface, with an oscillation frequency of  $6.5\text{ kHz}$  in the transverse direction and  $13\text{ Hz}$  in the longitudinal

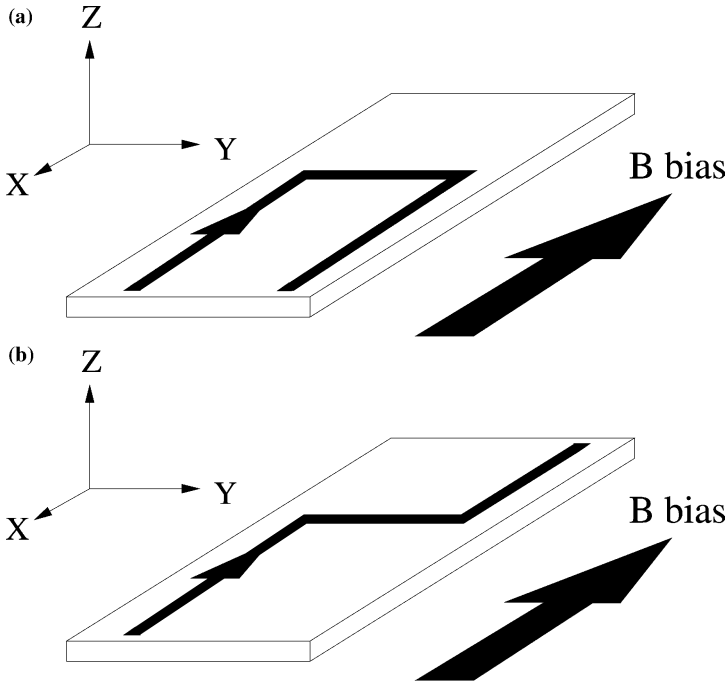


Fig. 4. Schematic diagrams of the U (upper) and Z (lower) wire trap configurations. The arrows on the chip surfaces indicate the direction of DC current flow; a uniform bias field is applied in the direction indicated. These two trapping wires are fabricated on the same chip, but shown separately here for clarity.

direction. These calculations are for  $^{40}\text{K}$ , and assume a 1 G “Ioffe field” applied in the  $\hat{y}$  direction, to increase the minimum field of the trap.

## 2.7. Sequencing

The experiment operates in a cycle, starting with the collection of hot atoms and progressively compressing and cooling the cloud to higher phase space density. Coordination of each stage of the experiment is accomplished using a dedicated real-time system sequencer.<sup>37</sup> The sequencer operates with an 80 MHz clock rate, and has 128 MB of onboard memory, allowing for the generation of complex waveforms. Twenty-four analog outputs and 32 digital outputs are updated as quickly as once every  $10\ \mu\text{s}$ . These outputs are buffered (as described below) and sent to various parts of the experiment: shutters, frequency modulators,

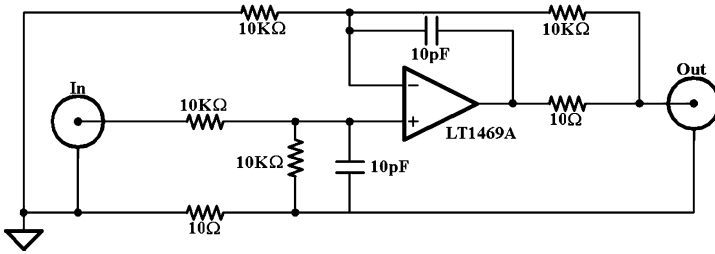


Fig. 5. Schematic diagram of one channel of the analog buffer.

power supplies, cameras, and the magnetic switch. A standard desktop computer programs the sequencer over an ethernet connection.

In order to protect the sequencer, drive low impedance loads, and prevent ground loops, buffers are used for all channels of the sequencer. Galvanic isolation of the digital channels is accomplished by using a GMR-based device.<sup>38</sup> The schematic used for the analog buffer is shown in Fig. 5. Outputs from the buffer have “soft” grounding: the  $10\Omega$  between the source ground and the buffer output return is low enough to carry any load current yet high enough to prevent ground loops. A variation on a differential input amplifier corrects for the output return’s offset and noise.

## 2.8. Evaporative Cooling System

Laser cooling of atoms is restricted to low densities because light must be able to escape from the cloud to carry away entropy. In essence, this constraint limits most laser cooling schemes to phase space densities below  $10^{-4}$ . Further cooling can be accomplished in a purely magnetic trap using evaporative cooling, in which the hottest atoms are selectively removed from the trap, each carrying away more than the average energy of a trapped atom. After rethermalization, the remaining ensemble has a lower temperature. Atoms are selectively removed using an electromagnetic field that couples only to atoms located at higher potential energy surfaces in the trap. Generally, the field is in the radio frequency (RF) range. The RF field spin-flips atoms to a magnetically anti-trapped state, and they are ejected from the trapping volume.

While many quantum gas experiments use standard commercial function generators, such devices typically have dwell times and switching times of 10 ms (or greater), rendering them unable to sweep quickly enough for an evaporation that may last only one second. Instead we generate the RF field using Direct Digital Synthesis (DDS), which has sufficient speed and precision for our application, at a fraction of the cost of a complete

high-frequency function generator. DDS creates a sinusoidal waveform point by point, which is then sent through a digital to analog converter.<sup>39</sup> Using dividers implemented in digital logic, any frequency from  $\mu\text{Hz}$  up to the Nyquist frequency (146 MHz in our case) can be generated with 48-bit resolution. Linear sweeps can be produced by specifying beginning and ending frequency, the number of frequency steps, and step time. Since no phase-locked loop is involved, the sweep rate is limited only by the digital clock cycle. Exponential sweeps are approximated piecewise by a series of linear sweeps.

The frequency and amplitude of the DDS are programmed using three digital lines from the sequencer. The RF output signal is amplified and fed into an auxiliary wire on the chip, which acts as an “antenna”. Since the antenna is less than a millimeter away from the atoms, little power is required to perform RF evaporation.

## 2.9. Imaging

We obtain information about the atom cloud with fluorescence and absorption imaging. Fluorescence imaging is accomplished by observing the light of a resonant laser beam scattered by an atom cloud. In absorption imaging, a resonant beam is passed through the cloud, and imaged on a CCD camera. The atoms absorb a portion of the laser beam, leaving behind a shadow of the atom cloud. Since the optical density of the cloud is proportional to the three-dimensional density integrated along the line of observation, the shadow gives direct information about the spatial distribution of the atom cloud.

At the chip, we also detect the cold atomic cloud by generating a one-dimensional Magneto-Optical Trap (1D MOT). A retro-reflected probe laser parallel to the chip surface is directed onto the magnetic field minimum of the chip trap, where the atoms are located. When the probe laser is red-detuned from resonance, the cold atomic cloud scatters light, while being confined by a magneto-optical forces in the direction of the probe propagation. The longer interrogation time in the 1D MOT allows for a higher signal-to-noise detection than simple fluorescence imaging. The method is useful for measuring atom number, but it does not image the cloud, since the atoms are pushed towards the magnetic center of the 1D MOT. (In fact, this technique is a useful way to determine the locations of magnetic field minima above the chip).

Four different imaging systems are used in the experiment: one looking from below along the  $\hat{z}$ -axis, two to image clouds at the chip from the  $\hat{x}$  and  $\hat{y}$  directions, and one to image the MOT and first magnetic trap. Each imaging system makes use of two lenses in order to form an image

of the cloud on the CCD of the camera. The two chip imaging systems are built to observe small clouds, and use a matched set of achromats with numerical apertures of 0.33 for the  $\hat{x}$ -axis system and 0.25 for the  $\hat{y}$ -axis system.

We use monochrome CCD cameras with  $640 \times 480$  pixels,  $7.4 \mu\text{m} \times 7.4 \mu\text{m}$  each, with a variable gain 10-bit intensity greyscale.<sup>40</sup> The acquisition duration is electronically shuttered and can be varied in steps of  $50 \mu\text{s}$ . Communication with imaging software over an IEEE1394 (“Fire-wire”) communication standard obviates the need for a dedicated imaging board.

### 3. TRAPPING OF $^{87}\text{Rb}$ AND $^{40}\text{K}$ ON A CHIP

Even though the experimental apparatus described in Section 2 is still in the final stages of construction and testing, we have successfully cooled and trapped atoms on the chip. In the following paragraphs we describe (in Section 3.1) the sequence we use for loading cold  $^{87}\text{Rb}$ , and (in Section 3.2) a recent result in which we have used a variation on the sequence to simultaneously load  $^{87}\text{Rb}$  and  $^{40}\text{K}$  into a chip trap.

#### 3.1. Experimental Sequence for $^{87}\text{Rb}$

From the background vapor produced by a rubidium dispenser, we trap and cool  $\sim 10^9$   $^{87}\text{Rb}$  atoms in a magneto-optical trap (MOT). The trapping beams each have an intensity of about  $2.5 \text{ mW/cm}^2$ , and are detuned  $\delta = -4.5\Gamma$  from the  $5S_{1/2}F=2 \rightarrow 5P_{3/2}F=3$  cycling transition. The repumper is 0.8% of the trapping intensity. The MOT coils provide a gradient of  $9 \text{ G/cm}$  along the strong axis. We cool the atoms further by rapidly turning off the current in the anti-Helmholtz coils and detuning the trapping beams to  $\delta = -9\Gamma$  for 9 ms to create an optical molasses. After this second cooling stage, we measure a temperature of  $T \leq 30 \mu\text{K}$  and a phase space density  $\rho \approx 3 \times 10^{-6}$ .

After the molasses stage, the atoms are recaptured in a purely magnetic trap with a vertical gradient of  $21 \text{ G/cm}$ . This magnetic field gradient is strong enough to trap atoms in the  $F=2$ ,  $m_F=2$  hyperfine ground state against the force of gravity, while atoms in lower magnetic substates remain untrapped. Once trapped, the atoms are compressed adiabatically for transport to the chip with a vertical gradient of  $47 \text{ G/cm}$  ( $94 \text{ G/cm}$  on the strong horizontal axis of the trap). Typically, we load 15% of the atoms ( $1.5 \times 10^8$  atoms) into the quadrupole trap, and after compression, they have a temperature of  $T \approx 100 \mu\text{K}$  and a phase space density of  $\rho \approx 10^{-7}$ .

The efficiency of the quadrupole trap loading is improved by the insertion of a short optical pumping step immediately after the optical molasses stage. We turn on a uniform bias magnetic field to provide a quantization axis for the atoms and then apply along this same axis a  $200\ \mu\text{s}$  laser pulse tuned to the  $5S_{1/2}F=2 \rightarrow 5P_{3/2}F=2$  transition to optically pump the atoms. By using  $\sigma+$  polarized light, the atoms are pumped into the  $F=2$ ,  $m_F=2$  hyperfine ground state. This step typically improves the loading efficiency by a factor of two, while leaving the size and temperature of the atomic cloud essentially unchanged.

We transport the atoms in the quadrupole trap up to the chip by changing the current in the Transfer coils. With a magnetic field gradient of  $47\ \text{G/cm}$  in the vertical direction, we move the atoms from the MOT position to the chip by smoothly varying the vertical ( $+\hat{z}$ ) bias magnetic field (produced by the Transfer coils) from  $-84$  to  $+121\ \text{G}$  in about  $600\ \text{ms}$ . The atoms do not experience any significant loss or heating during the transport. Horizontal ( $\hat{x}$  and  $\hat{y}$ ) bias magnetic fields provide transverse positioning to align the cloud to the center of the  $\mu\text{EM}$  trap.

Once at the chip, the atoms are loaded into the U-wire trap by first increasing the current in the U-wire, and then simultaneously decompressing the quadrupole trap while increasing the transverse horizontal bias magnetic field for the chip trap. The loading process takes  $300\ \text{ms}$ . After loading the U-wire trap, we find that the trap contains  $1 \times 10^7$  atoms with a temperature of  $T = 200\ \mu\text{K}$  and a phase space density of  $\rho \approx 10^{-7}$ .

This entire sequence can be initiated at a lower vapor pressure by turning off the dispensers and using LIAD, as is described in Section 2.2. Figure 6 shows images of light-desorbed  $^{87}\text{Rb}$  in the MOT (Fig. 6a) and after release from the chip trap (Fig. 6b and c).

### 3.2. Simultaneous Loading of $^{87}\text{Rb}$ and $^{40}\text{K}$

Recently, we have adapted the above sequence, developed for  $^{87}\text{Rb}$ , to include  $^{40}\text{K}$ . We report two technical milestones: (1) trapping of a cold fermionic atomic species in a chip trap, and (2) simultaneous trapping of two elements, in this case a bosonic isotope and a fermionic isotope, in a chip trap.

In order to load  $^{40}\text{K}$  onto the chip, we make the following changes to the sequence. We turn on the  $^{40}\text{K}$ -enriched dispenser and potassium lasers to load a MOT. Then, instead of using an optical molasses cooling stage, we compress the MOT for  $100\ \text{ms}$  with an anti-Helmholtz gradient of  $94\ \text{G/cm}$ . The trapping beams are then turned off and the atoms remain trapped in the magnetic quadrupole field (which is already on at full

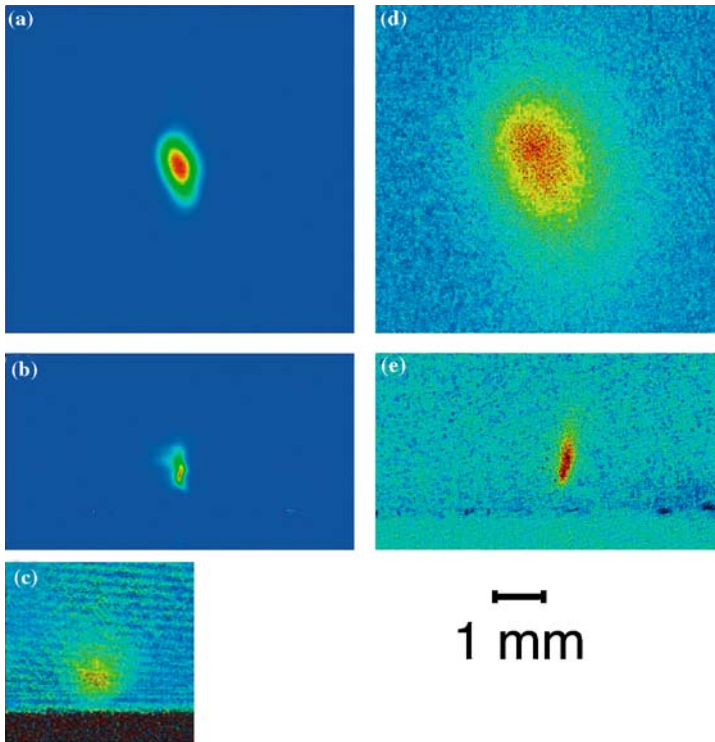


Fig. 6. Images of  $^{87}\text{Rb}$  (left column) and  $^{40}\text{K}$  (right column) clouds in the magneto-optical trap and-at the chip: (a)  $^{87}\text{Rb}$  MOT; (b)  $^{87}\text{Rb}$  after  $\mu\text{EM}$  trapping, imaged using a 1D MOT at the chip; (c) Absorption image of  $^{87}\text{Rb}$  after release from the  $\mu\text{EM}$  trap; (d)  $^{40}\text{K}$  MOT; (e)  $^{40}\text{K}$  after  $\mu\text{EM}$  trapping, imaged using a 1D-chip-MOT fluorescence detection scheme described in Section 2.9. More detail about atom numbers and imaging techniques are given in the text. All images use the same spatial scale, which is indicated.

strength). The rest of the sequence is as described in Section 3.1: we transport the cold atoms to the chip and transfer them into the  $\mu\text{EM}$  trap.

Using this sequence,  $^{40}\text{K}$  is loaded onto the chip. Figure 6d shows a  $^{40}\text{K}$  MOT and Fig. 6e shows a  $^{40}\text{K}$  cloud that was released from the  $\mu\text{EM}$  trap and imaged using the 1D-chip-MOT fluorescence detection scheme described in Section 2.9.

Turning on the LIAD source and  $^{87}\text{Rb}$  lasers, we observe that *both* species are loaded onto the chip, although  $^{87}\text{Rb}$  is not loaded as efficiently as in the original sequence. By selecting a probe beam at 780 or 767 nm, we can detect  $^{87}\text{Rb}$  or  $^{40}\text{K}$  atoms, independently. We observe simultaneous



trapping of  $2 \times 10^5$   $^{87}\text{Rb}$  atoms and  $6 \times 10^4$   $^{40}\text{K}$  atoms in the U-wire trap.

### 3.3. Discussion and Future Work

While the above sequences are successful, they are not optimal. The transfer efficiency ( $\sim 10\%$ ) from the external quadrupole trap to the U-wire  $\mu\text{EM}$  trap is not as high as has been previously observed in similar transfer sequences.<sup>13</sup> It is possible that we are limited by the trap depth of the  $\mu\text{EM}$  trap.

The sequence used to load  $^{40}\text{K}$  is preliminary and has not been studied carefully. Unlike the sequence described in Section 3.1. the method described in Section 3.2 to load the magnetic trap will trap more than one  $m_F$  level in each species. A spin mixture in the magnetic trap is susceptible to spin exchange losses. The range of magnetic sublevels can be reduced with an optical pumping step.

Future work includes the evaporative cooling of  $^{87}\text{Rb}$  and sympathetic cooling of  $^{40}\text{K}$ , both to quantum degeneracy. For quantum degeneracy, atoms must be loaded into the Z-wire trap, whose Ioffe-Pritchard field configuration avoids spin-flip losses. Improvements in loading the chip will be necessary to achieve the correct starting condition for evaporative cooling to degeneracy.

Several additions to our apparatus are possible. Manipulation of the atoms with microwaves will enable the simultaneous evaporation of  $^{40}\text{K}$  and  $^{87}\text{Rb}$ , which has been shown to improve efficiency in other dual species experiments.<sup>41</sup> Far off-resonant laser light can be used to form a trap using the induced electric dipole of the atom. Such an optical trap is useful for the study of multiple spin states, and for accessing Feshbach-Verhaar resonances.<sup>42</sup> A next-generation microfabricated trap will be built to reduce light scattering off the chip, and to address known problems with the techniques used to fabricate our chip.<sup>18</sup> Finally, a higher quality camera will improve our imaging sensitivity.

## 4. CONCLUSION

In conclusion, we have demonstrated the trapping of  $^{40}\text{K}$  and of  $^{87}\text{Rb}$  on a chip. To our knowledge, this is the first time fermions have been confined by a  $\mu\text{EM}$  trap, and the first time two elements have been simultaneously loaded into a  $\mu\text{EM}$  trap. The apparatus used to achieve this has been described in detail, indicating some technical choices that may interest researchers in the field.

The high aspect ratio of these traps may be useful for studies of quasi-one-dimensional ensembles. In the simplest case, the aspect ratio is controlled by the ratio of the wire current to the bias field: the closer the trap is to the surface, the higher its aspect ratio. The 500:1 aspect ratio of the Z-trap in the example given in Section 2.6. seems well suited to quasi-one-dimensional experiments. A complication is the trap “roughness,” which has been investigated in Refs. 12, 18. This roughness may spoil the use of some wire traps as simple elongated traps, but may also allow for the study of quantum gases in potentials with frozen-in randomness.<sup>43</sup>

*Note added in proof.* Since the original submission of this paper, we have been able to load simultaneously  $2 \times 10^{-7}$   $^{87}\text{Rb}$  atoms with a phase space density of  $3 \times 10^{-6}$ , along with  $2 \times 10^{-5}$   $^{40}\text{K}$  atoms in the  $|F = 9/2, m_F = 9/2\rangle$  state into the z-wire trap.

## ACKNOWLEDGMENTS

We would like to thank Hyun Youk and Ryan Bolen for early work on this project. We also thank Thorsten Schumm, Brian DeMarco, Vladan Vuletić, Peter Krüger, Sebastian Hoferberth, Jörg Schmiedmayer, and Jozsef Fortágh for stimulating and helpful conversations. S.A. and L.L. acknowledge support from NSERC; M.H.T.E. acknowledges support from OGS. This work was supported by CFI, OIT, NSERC, PRO, and Research Corporation.

## REFERENCES

1. M. H. Anderson, J. R. Ensher, M. R. Matthews, C. E. Wieman, and E. A. Cornell, *Science* **269**, 198 (1995); K. B. Davis, M.-O. Mewes, M. R. Andrews, N. J. van Druten, D. S. Durfee, M. Kurn, and W. Ketterle, *Phys. Rev. Lett.* **75**, 3969 (1995); C. C. Bradley, C. A. Sackett, J. J. Tollett, and R. G. Hulet, *Phys. Rev. Lett.* **75**, 1687 (1995); see also C. A. Sackett, C. C. Bradley, M. Welling, and R. G. Hulet, *Appl. Phys. B* **B65**, 433 (1997).
2. B. DeMarco and D. S. Jin, *Science* **285**, 1703 (1999); A. G. Truscott, K. E. Strecker, W. I. McAlexander, G. B. Partridge, and R. G. Hulet, *Science* **291**, 2570 (2001); F. Schreck, L. Khaykovich, K. L. Corwin, G. Ferrari, T. Bourdel, J. Cubizolles, and C. Salomon, *Phys. Rev. Lett.* **87**, 080403 (2001); S. R. Granade, M. E. Gehm, K. M. O’Hara, and J. E. Thomas, *Phys. Rev. Lett.* **88**, 120405 (2002); Z. Hadzibabic, C. A. Stan, K. Diechmann, S. Gupta, M. W. Zwierlein, A. Görlitz, and W. Ketterle, *Phys. Rev. Lett.* **88**, 160401 (2002); G. Roati, F. Riboli, G. Modugno, and M. Inguscio, *Phys. Rev. Lett.* **89**, 150403 (2002); M. Bartenstein, A. Altmeyer, S. Riedl, S. Jochim, C. Chin, J. Hecher Denschlag, and R. Grimm, *Phys. Rev. Lett.* **92**, 120401 (2004); M. Köhl, H. Moritz, T. Stöferle, K. Günter, T. Esslinger *Phys. Rev. Lett.* **94**, 080403 (2005); C. Silber, S. Guenther, C. Marzok, B. Deh, Ph. W. Courteille, C. Zimmermann. cond-mat/0506217; C. Ospelkaus, S. Ospelkaus, H. Sengstoch, K. Bongs cond-mat/0507219.

3. W. Hofstetter, J. I. Cirac, P. Zoller, E. Demler, and M. D. Lukin, *Phys. Rev. Lett.* **89**, 220407 (2002).
4. U. Gavish and Y. Castin, *Phys. Rev. Lett.* **95**, 020401 (1995).
5. C. A. Regal, M. Greiner, and D. S. Jin, *Phys. Rev. Lett.* **92**, 040403 (2004); M. Bartenstein, A. Altmeyer, S. Riedl, S. Jochim, C. Chin, J. Hecker Denschlag, and R. Grimm, *Phys. Rev. Lett.* **92**, 120401 (2004); T. Bourdel, L. Khaykovich, J. Cubizolles, J. Zhang, F. Chevy, M. Teichmann, L. Tarruell, S. J. J. M. F. Kokkelmans, C. Salomon, *Phys. Rev. Lett.* **93**, 050401 (2004); M. W. Zwierlein, C. A. Stan, C. H. Schunck, S. M. F. Raupach, A. J. Kerman, W. Ketterle, *Phys. Rev. Lett.* **92**, 120403 (2004).
6. W. Hänsel, P. Hommelhoff, T. W. Hänsch, and J. Reichel, *Nature* **413**, 498 (2001).
7. H. Ott, J. Fortagh, G. Schlotterbeck, A. Grossmann, and C. Zimmermann, *Phys. Rev. Lett.* **87**, 230401 (2001).
8. J. D. Weinstein and K. G. Libbrecht, *Phys. Rev. A*, **52**, 4004 (1995).
9. J. H. Thywissen, M. Olshanii, G. Zabow, M. Drndić, K. S. Johnson, R. M. Westervelt, and M. Prentiss, *Eur. Phys. J. D* **7**, 361 (1999); D. Müller, D. Z. Anderson, R. J. Grow, P. D. D. Schwindt, and E. A. Cornell, *Phys. Rev. Lett.* **83**, 5194 (1999); N. H. Dekker, C. S. Lee, V. Lorent, J. H. Thywissen, S. P. Smith, M. Drndić, R. M. Westervelt, and M. Prentiss, *Phys. Rev. Lett.* **84**, 1124 (2000).
10. W. Hänsel, J. Reichel, P. Hommelhoff, and T. W. Hänsch, *Phys. Rev. Lett.* **86**, 608 (2001).
11. R. Folman, P. Krüger, D. Cassettari, B. Hessmo, T. Maier, and J. Schmiedmayer, *Phys. Rev. Lett.* **84**, 4749 (2000).
12. J. Fortágh, H. Ott, S. Kraft, A. Günther, and C. Zimmermann, *Phys. Rev. A* **66**, 041604(R) (2002); M. P. A. Jones, C. J. Vale, D. Sahagun, B. V. Hall, and E. A. Hinds, *Phys. Rev. Lett.* **91**, 080401 (2003); J. M. McGuirk, D. M. Harber, J. M. Obrecht, and E. A. Cornell, *Phys. Rev. A* **69**, 062905 (2004).
13. Y. Lin, I. Teper, C. Chin, and V. Vuletić, *Phys. Rev. Lett.* **92**, 050404 (2004).
14. J. Schneider and F. Wallis, *Phys. Rev. A* **57**, 1253 (1998).
15. B. E. Granger and D. Blume, *Phys. Rev. Lett.* **92**, 133202 (2004).
16. K. Das, *Phys. Rev. Lett.* **90**, 170403 (2003); M. A. Cazalilla and A. F. Ho, *Phys. Rev. Lett.* **91**, 150403 (2003).
17. J. H. Thywissen, R. M. Westervelt, and M. Prentiss, *Phys. Rev. Lett.* **83**, 3762 (1999).
18. J. Estève, C. Aussibal, T. Schumm, C. Figl, D. Mailly, I. Bouchoule, C. I. Westbrook, and A. Aspect, *Phys. Rev. A* **70**, 043629 (2004).
19. S. Du, M. B. Squires, Y. Imai, L. Czaia, R. A. Saravanan, V. Bright, J. Reichel, T. W. Hänsch, and D. Z. Anderson, *Phys. Rev. A* **70**, 053606 (2004).
20. See, for instance, W. Ketterle, D. S. Durfee, and D. M. Stamper-Kurn, in *Bose-Einstein condensation in atomic gases. Proceedings of the International School of Physics "Enrico Fermi"*, Course CXL, M. Inguscio, S. Stringari, and C. E. Wieman (eds.), IOS Press, Amsterdam, (1999) pp. 67–176 (cond-mat/9904034). A more detailed description of one BEC experiment is given in H. J. Lewandowski, D. M. Harber, D. L. Whitaker, and E. A. Cornell, *J. Low Temp. Phys.* **132**, 309 (2003).
21. J. E. Bjorkholm, *Phys. Rev. A* **38**, 1599 (1988).
22. Radiative transfer is unaffected by the vacuum, but not significant because the absorption frequencies of ground-state alkali atoms are far above the emission range of a blackbody at room temperature.
23. The ion pump is a Varian VacIon Plus 75 StarCell pump (751/s); the sublimation pump uses a Varian 8" CF Cryopanel; the turbo pump used is a Pfeiffer Vacuum TMU071P; the gate valve used is a VAT 10836-UE44-0005 DN63 2-1/2".
24. C. Wieman, G. Flowers, and S. Gilbert, *Am. J. Phys.* **63**, 317 (1995); J. Fortagh, A. Grossmann, T. W. Hänsch, and C. Zimmermann, *J. Appl. Phys.* **84**, 6499 (1998).
25. Alkali metal dispensers are available from SAES Getters.
26. B. DeMarco, H. Rohner, and D. S. Jin, *Rev. Sci. Instr.* **70**, 1967 (1999).
27. A. Gozzini, F. Mango, J. H. Xu, G. Alzetta, F. Maccarrone, and R. A. Bernheim, *Il Nuovo Cimento* **15**, 709 (1993).

28. M. Meucci, E. Mariotti, P. Bicchi, C. Marinelli, and L. Moi, *Europhys. Lett.* **25**, 639 (1994).
29. B. P. Anderson and M. A. Kasevich, *Phys. Rev. A* **63**, 023404 (2001).
30. LIAD is also effective for both  $^{39}\text{K}$  and  $^{40}\text{K}$ , but we have not studied this efficiency as a function of wavelength.
31. Leaving the dispensers off for several weeks, we observe a slow decay in the atom number in the MOT, as if a diminishing amount of  $^{87}\text{Rb}$  is accessible to desorption. This behavior has also been observed by Dana Anderson and coworkers at JILA.
32. J. Goldwin, S. B. Papp, B. DeMarco, and D. S. Jin, *Phys. Rev. A* **65**, 021402 (2002).
33. These dichroic waveplates act as a  $\lambda/2$  waveplate for 780 nm and a  $\lambda$  waveplate for 767 nm. They were designed and custom built by OptiSource LLC.
34. The wire is hollow to allow the flow of pressurized cooling water through the centre of the wire. It was manufactured by Wolverine Fabricated Products and insulated by S&W Wire.
35. W. Ketterle and N. J. van Druten, *Adv. At. Mol. Opt. Phys.* **37**, 181 (1996).
36. S. Groth, P. Krüger, S. Wildermuth, R. Folman, T. Fernholz, D. Mahalu, I. Bar-Joseph, and J. Schmied-mayer, cond-mat/0404141 (2004).
37. We use an ADwin Pro sequencer, from Jäger Computergesteuerte Messtechnik GmbH.
38. Isolation for both inputs and outputs is done by the NVE 1L715-3 quad GMR-based device. The Texas Instruments SN64BCT25244NT octal buffer gives a tolerant  $50\ \Omega$  output to the array of BNC connectors.
39. The DDS chip we use is the Analog Device's AD9854, and comes on an evaluation board costing roughly US \$200. In our implementation, an on-board 15.360 MHz reference oscillator is multiplied up 19 times to give a 291.84 MHz sample frequency.
40. MicroPix cameras are used (model M640), with the window covering the CCD chip removed by the manufacturer.
41. K. E. Strecker, G. B. Partridge, and R. G. Hulet, *Phys. Rev. Lett.* **91**, 080406 (2003).
42. E. Tiesinga, B. J. Verhaar, and H. T. C. Stoof, *Phys. Rev. A* **47**, 4114 (1993); S. Inouye, M. R. Andrews, J. Stenger, H.-J. Miesner, D. M. Stamper-Kurn, and W. Ketterle, *Nature* **392**, 151 (1998); J. L. Roberts, N. R. Claussen, J. P. Burke, Jr., Chris H. Greene, E. A. Cornell, and C. E. Wieman, *Phys. Rev. Lett.* **81**, 5109 (1998).
43. D. Wang, M. D. Lukin, and E. Demler, *Phys. Rev. Lett.* **92**, 076802 (2004).